AGU PUBLICATIONS

Geophysical Research Letters

RESEARCH LETTER
10.1002/2017GL073980

Key Points:
- Hybrid simulations of solar wind plasma interaction with magnetized or conductive asteroid Psyche
- Magnetized and conductive cases for Psyche show significant differences in solar wind interaction
- We provide predictions for Discovery mission to Psyche with implications for the formation history of Psyche

Supporting Information:
- Supporting Information S1

Correspondence to:
S. Fatemi,
shahab@irf.se;
shahabfatemi@gmail.com

Citation:
Fatemi, S., & Poppe, A. R. (2018). Solar wind plasma interaction with asteroid 16 Psyche: Implication for formation theories. *Geophysical Research Letters*, *45*. https://doi.org/10.1002/2017GL073980

Received 28 APR 2017
Accepted 22 NOV 2017
Accepted article online 30 NOV 2017

Solar Wind Plasma Interaction with Asteroid 16 Psyche: Implication for Formation Theories

Shahab Fatemi[1,2,3] and Andrew R. Poppe[2,3]

[1]Swedish Institute of Space Physics, Kiruna, Sweden, [2]Space Sciences Laboratory, University of California at Berkeley, Berkeley, CA, USA, [3]Solar System Exploration Research Virtual Institute, NASA Ames Research Center, Mountain View, CA, USA

Abstract The asteroid 16 Psyche is a primitive metal-rich asteroid that has not yet been visited by spacecraft. Based on remote observations, Psyche is most likely composed of iron and nickel metal; however, the history of its formation and solidification is still unknown. If Psyche is a remnant core of a differentiated planetesimal exposed by collisions, it opens a unique window toward understanding the cores of the terrestrial bodies, including the Earth and Mercury. If not, it is perhaps a reaccreted rubble pile that has never melted. In the former case, Psyche may have a remanent, dipolar magnetic field; in the latter case, Psyche may have no intrinsic field, but nevertheless would be a conductive object in the solar wind. We use Advanced Modeling Infrastructure in Space Simulation (AMITIS), a three-dimensional GPU-based hybrid model of plasma that self-consistently couples the interior electromagnetic response of Psyche (i.e., magnetic diffusion) to its ambient plasma environment in order to quantify the different interactions under these two cases. The model results provide estimates for the electromagnetic environment of Psyche, showing that the magnetized case and the conductive case present very different signatures in the solar wind. These results have implications for an accurate interpretation of magnetic field observations by NASA's Discovery mission (Psyche mission) to the asteroid 16 Psyche.

1. Introduction

Among the diverse populations of asteroids, 16 Psyche is a massive metallic (M-type) asteroid located at approximately 3 AU (astronomical units) in the main asteroid belt (e.g., Bell et al., 1989; Magri et al., 1999; Shepard et al., 2008; Zellner and Gradie, 1976). Radio telescope observations have indicated that Psyche mainly consists of iron and nickel metal and have estimated its bulk density variously to be 1800 ± 600 kg/m^3 (Viateau, 2000), $3,300 \pm 700$ kg/m^3 (Lupishko, 2006), and $7,600 \pm 3,000$ kg/m^3 (Shepard et al., 2008). Psyche may also have significant macroporosity, with estimates ranging from ~30% to ~70% (Britt et al., 2002; Lupishko, 2006; Shepard et al., 2017). In addition, Psyche's high radar albedo of 0.37–0.42 (Shepard et al., 2010, 2017) and high thermal inertia of ~120 J m^{-2}S$^{-0.5}$K^{-1} (Matter et al., 2013) are indicative of a metallic nature (Elkins-Tanton et al., 2016). Radar observations have estimated Psyche's shape to be ellipsoidal with dimensions $279 \times 232 \times 189$ km (±10%) and average diameter of 226 ± 15 km (radius of $\sim 113 \pm 7$ km) (Shepard et al., 2017) and have indicated a rotational period of approximately 4.2 h (e.g., Kaasalainen et al., 2002). Despite these measurements, the exact physical properties of Psyche are still unknown, mainly due to the lack of short-range observations of either Psyche or other M-type asteroids.

Generally, two plausible scenarios exist for the formation and solidification of Psyche with distinct conclusions regarding its current state. The most accepted scenario suggests that Psyche is a remnant core of an ancient differentiated planetesimal exposed by hit-and-run collisions (e.g., Asphaug et al., 2006; Elkins-Tanton et al., 2015, 2016; Elkins-Tanton, 2016). If Psyche was initially molten or melted later by repeated impacts, Psyche may possess remnant magnetic fields associated with a core dynamo (Elkins-Tanton et al., 2016). The second scenario argues that Psyche is not a planetary core but is instead a reaccreted rubble pile of remnants from one or more of the collisions that impacted the parent planetesimal (e.g., Britt et al., 2002; Bottke et al., 2006; Davis et al., 1999). This latter scenario suggests that Psyche has never melted, and thus, no dynamo formed (e.g., Elkins-Tanton et al., 2016).

Similar to other terrestrial objects, Psyche is exposed to the solar wind; however, the solar wind interaction with an object of Psyche's size that is also highly conductive and perhaps magnetized represents a unique

class of interaction, different from other previously studied terrestrial objects, such as the Moon (e.g., Halekas et al., 2015; Holmström et al., 2012; Ogilvie et al., 1996), Mercury (e.g., Jia et al., 2015; Kabin et al., 2000; Russell, 1979; Raines et al., 2015) or asteroids 1 Ceres (e.g., Kallio et al., 2008; Lindkvist et al., 2017), 951 Gaspra, and 243 Ida (e.g., Blanco-Cano et al., 2003; Kivelson et al., 1995; Omidi et al., 2002; Wang et al., 1995). As will be shown here, Psyche's electromagnetic environment provides significant data with respect to its magnetic properties, which in turn constrains various theories regarding its formation and evolution. Previous simulations and theoretical calculations have studied the solar wind plasma interaction with asteroids of various sizes, shapes, and magnetization levels (e.g., Baumgärtel et al., 1997; Blanco-Cano et al., 2003; Kivelson et al., 1995; Omidi et al., 2002; Richter et al., 2012; Simon et al., 2006; Wang et al., 1995; Wang & Kivelson, 1996; Zimmerman et al., 2014). They have either focused on the interaction with a highly magnetized asteroid, like 951 Gaspra and 243 Ida (Baumgärtel et al., 1994, 1997; Blanco-Cano et al., 2003; Kivelson et al., 1995; Omidi et al., 2002; Simon et al., 2006; Wang et al., 1995; Wang & Kivelson, 1996), or with an unmagnetized nonconductive asteroid, like 1 Ceres (e.g., Kallio et al., 2008; Lindkvist et al., 2017). However, no peer-reviewed studies have been published previously on the solar wind interaction with a conductive asteroid in the solar wind, nor on the solar wind interaction with an asteroid of Psyche's size. Importantly, the small characteristic length scales of asteroids, including Psyche, require the use of kinetic plasma models in order to investigate their interaction with the solar wind. Magnetohydrodynamics would not be able to explain this interaction as long as the solar wind ion gyroradius is larger or comparable to the interaction size.

NASA's newly announced Discovery mission (the Psyche spacecraft Elkins-Tanton et al., 2016, 2017; Oh et al., 2016) will visit 16 Psyche for the first time (planned launch in 2022 and arrival at Psyche in 2026 Oh et al., 2016; Elkins-Tanton et al., 2016) and will carry on board a magnetometer (among other instruments). Here we use a GPU-based (Graphical Processing Unit) three-dimensional hybrid model of plasma (kinetic ions and fluid electrons) that self-consistently couples the electromagnetic interior response of an object (i.e., magnetic diffusion) with its ambient plasma and electromagnetic field (Fatemi et al., 2017). We study the solar wind plasma interaction with Psyche, assuming the asteroid is either magnetized and insulating or unmagnetized yet highly conductive and examine the possible magnetic signatures to be observed. These results provide predictions for magnetometer measurements by NASA's Psyche mission with implications for the formation and solidification of a metal world.

2. Model

We use the AMITIS simulation code, the first parallel GPU-based three-dimensional (3-D in both configuration and phase space) hybrid plasma model that uses a single CPU-GPU pair (Fatemi et al., 2017). This model, in addition to improvements in solving the hybrid model equations for conductive bodies, does not require access to high-performance computing facilities as it uses only a single CPU and a single GPU yet runs at least 10 times faster and is more energy and cost efficient compared to similar parallel CPU-based models (Fatemi et al., 2017). In this model, the ions are charged macroparticles, electrons are a massless charge-neutralizing fluid, and electromagnetic fields are self-consistently computed from Maxwell's equations. In addition, AMITIS allows the definition of custom electrical conductivity profiles for the interior of an object and self-consistently couples the interior magnetic response to the ambient plasma environment using an implicit-explicit method (model details are extensively explained in Fatemi et al., 2017).

2.1. Coordinate System and Simulation Parameters

For all simulations, we use a right-handed coordinate system centered at Psyche. The solar wind flows along the $-x$ axis, the $+z$ axis is perpendicular to the ecliptic plane and points toward ecliptic north, and the y axis completes the right-hand system. We use typical solar wind parameters at 3 AU (the mean heliocentric distance of Psyche from the Sun): the plasma density is 2 cm^{-3}, solar wind speed is 400 km/s and is flowing along the $-x$ axis, the ion and electron temperatures are ~6 eV and ~8 eV, respectively, and the magnitude of the interplanetary magnetic field (IMF) is 2 nT. Thus, the ion sound speed is $c_s \approx 48$ km/s (sonic Mach number is $M_S \approx 8.3$), Alfvén speed is $v_A \approx 31$ km/s (Alfvén Mach number is $M_A \approx 12.9$), plasma beta (the ratio between plasma pressure and magnetic pressure) is $\beta_i \approx 2.8$, ion thermal gyroradius is $r_{gi} \approx 175$ km, solar wind ram pressure is $p_{sw} \approx 0.54$ nPa, ion skin depth (inertial length) is $\delta_i = c/\omega_{pi} \approx 161$ km, and electron skin depth is $\delta_e = c/\omega_{pe} \approx 3.7$ km. At the orbit of Psyche, the direction of the IMF is on average quasi-perpendicular (~75°) to the solar wind flow following the Parker spiral. However, to provide a simpler interpretation for our simulation results we assume that the IMF is perpendicular (90°) to the solar wind flow and is along the $+z$ axis. Therefore, the solar wind convective electric field ($-\mathbf{v} \times \mathbf{B}$) is 0.8 mV/m and is along the $-y$ axis.

Table 1
Magnetic Dipole and Interior Conductivity Applied in our Simulations

Run	Conductivity[a] (S/m)	Dipole moment (A m^2)	Dipole orientation[b] ($\hat{M}_x, \hat{M}_y, \hat{M}_z$)	Intrinsic surface field strength[c] (nT)
#1	10^{-7}	2.5×10^{15}	(0, 0, −1)	∼145
#2	10^{-7}	1.0×10^{16}	(0, 0, −1)	∼580
#3	10^{+1}	0.0	N/A	N/A

[a]Uniform electrical conductivity applied everywhere inside Psyche with radius $R_\Psi = 120$ km. [b]$\hat{M}_i$ is dipole moment unit vector along the *i* axis. [c]Magnitude of the magnetic field on the surface at $(x, y, z) = (+1, 0, 0)R_\Psi$.

The surface of Psyche is modeled as a perfect plasma absorber such that when a particle impacts the surface, it is immediately removed from the simulation.

We use regular-spaced Cartesian cubic grids of size $R_\Psi/6$, where $R_\Psi = 120$ km is the approximate mean radius of Psyche ($R_\Psi \approx 0.75\delta_i$ or $\approx 0.7r_{gi}$). Generally, in a hybrid model of plasma the simulation cell size needs to be much larger than electron inertial length (e.g., Ledvina et al., 2008, and references therein). Thus, we have chosen our simulation cell sizes to be 20 km ($5.5\delta_e$). We also examined the effects of cell sizes in our simulation results by taking smaller grid cells (10 km $\approx 2.2\delta_e$). Although we did not observe any noticeable differences between our higher grid resolution simulations compared to those with lower resolution (20 km), the results from simulations with 20 km cell sizes are presented here because the 10 km cell size simulations for Psyche are computationally too expensive even using GPUs and may result in nonphysical results (see supporting information for more details).

Although Psyche is ellipsoidal, we assume it is a spherical object in this study for simplicity. Each grid cell is initially loaded with 16 protons (macroparticles) with a drifting Maxwellian velocity distribution and uniform electric and magnetic fields at the beginning of a simulation ($t = 0$ s). The particles are continuously injected into the simulation domain from $x = +8R_\Psi$ and are removed from the simulation at the out flow boundary at $x = -8R_\Psi$. The four other boundaries are periodic. We present the results after the simulations reach steady state solution ($t \geq 30$ s, when the electromagnetic fields and plasma density and velocity do not have any considerable changes in time), with the exception of simulation run #3, discussed in detail below and in section 3.

One of the fundamental assumptions of our model, which is typical for the majority of hybrid models, is considering electrons as a massless charge-neutralizing fluid. The electron gyroradius for the plasma parameters used in our simulation (typical at 3 AU) is <1.2 km, which is $<10^{-2}R_\Psi$. Therefore, the fluid assumption of electrons and their interaction with a Psyche sized object is a valid assumption. However, comparison between the hybrid simulation results presented in section 3 and a full electromagnetic particle in cell that assumes realistic solar wind proton and electron masses with realistic assumptions on the size of the asteroid and on the speed of light would be very interesting for space plasma and planetary science communities.

2.2. Simulation Runs and Motivations

As listed in Table 1, we conducted three simulation runs using the upstream plasma parameters described in section 2.1. For simulation runs #1 and #2, Psyche is assumed to be a remnant core of a differentiated planetesimal exposed by hit-and-run collisions. For these runs, we model Psyche as an electrically resistive obstacle with uniform interior conductivity 10^{-7} S/m and an intrinsic magnetic dipole. Psyche's magnetization, conductivity, and interior structure are still unknown. However, the dipole moments assumed in runs #1 and #2 are within the ranges suggested by Greenstadt (1971), Auster et al. (2010), and Weiss et al. (2016) for an asteroid of radius 120 km. The relatively low interior conductivity in these runs allows us to investigate the solar wind interaction with a magnetized Psyche without concerns about induced magnetic fields generated from its interior. We set the orientation of the magnetic dipole moment to be along the $-z$ axis (antiparallel to the IMF) and set the surface magnetic field strength at the magnetic equator of Psyche (in the *xy* plane) to ∼145 nT and ∼580 nT for runs #1 and #2, respectively. For run #3, Psyche is assumed to be an unmagnetized but highly conductive obstacle to the solar wind. We already know that metal has a higher conductivity compared to silicate and also we know that the conductivity of the Earth's core is on the order of 10^{+6} S/m (e.g., Gomi & Hirose, 2015; Stacey & Anderson, 2001). Moreover, measurement of pure iron and nickel metals

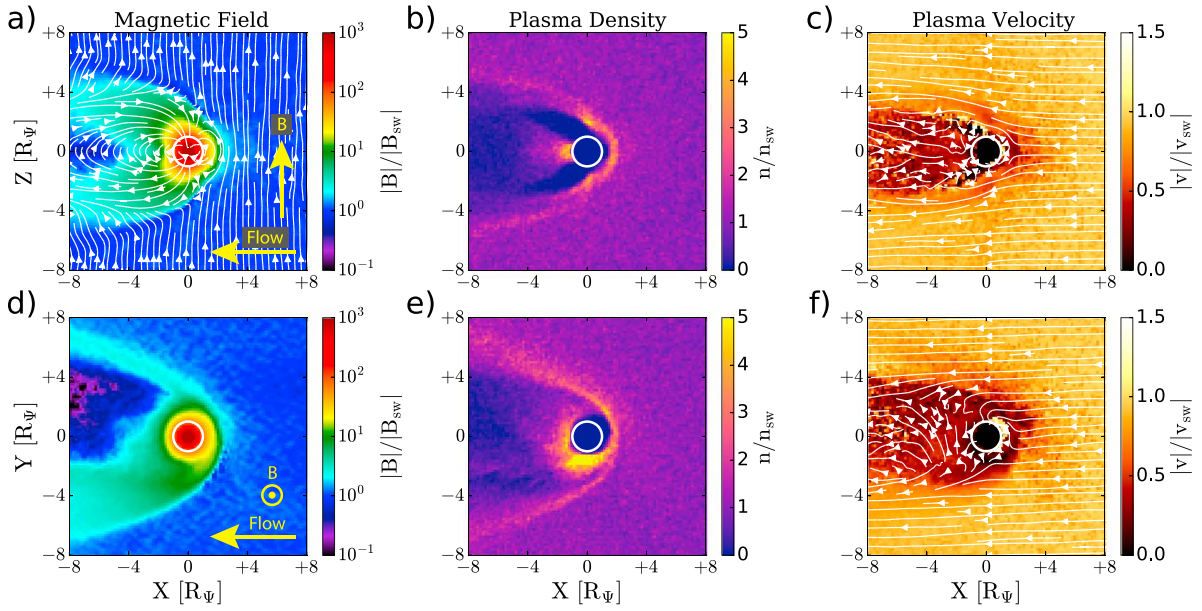

Figure 1. Hybrid simulation results for run #1 presented in Table 1. (a and d) Magnitude of the magnetic field normalized to the undisturbed upstream magnetic field B_{sw} = 2 nT; (b and e) proton number density normalized to the upstream solar wind number density n_{sw} = 2 cm^{-3}; and (c and f) plasma velocity normalized to upstream solar wind speed v_{sw} = 400 km/s. Streamlines show the magnetic field line tracing in Figure 1a and the plasma flow vectors in Figures 1c and 1f. Figures 1a–1c are cuts in the *xz* plane at $y = 0$, and Figures 1d–1f are cuts in the *xy* plane at $z = 0$. We assume Psyche is a spherical object and is shown by a circle, centered at the origin of the coordinate system. The axes are in the unit of Psyche's radius R_Ψ and the plasma flow and the IMF direction are shown by arrows.

in the laboratory environment gives an estimate of their conductivity of a similar order (e.g., Banaszkiewicz et al., 2007; Fert & Campbell, 1976). Taking into account the size, mass density, macroporosity, and thermal conductivity of Psyche, which are estimated using remote observations explained in the introduction, an interior conductivity within a broad range of 10^{-2}–10^{+4} S/m is expected for a metallic asteroid like Psyche. Therefore, in run #3, we assume Psyche has a uniform electrical conductivity of 10 S/m. This run allows us to examine the second scenario for Psyche's formation, namely, a conductive metallic object that never melted and thus does not possess remanent magnetic fields.

3. Results

Figure 1 shows the hybrid simulation results for run #1, where the equatorial surface field is ~145 nT. In general, a magnetospheric-like structure forms around Psyche. Figure 1a shows that the intrinsic magnetic fields of Psyche are compressed upstream by the solar wind pressure forming a magnetopause and magnetosheath-like region upstream and a magnetotail structure downstream. Figure 1b shows that the solar wind plasma is also compressed upstream of the magnetopause as well as in the magnetic cusps and forms a low-density region inside Psyche's magnetosphere, similar to terrestrial planetary magnetospheres. A notable feature in Figure 1b is a high plasma density region at low-latitudes downstream near the anti subsolar point ($x < -R_\Psi$). This structure is formed by solar wind ions that become quasi-trapped inside Psyche's magnetosphere and undergo bounce and drift motion. The simulation results suggest that this structure is permanent as long as the solar wind and IMF do not considerably change upstream. Figure 1c shows that the solar wind plasma is decelerated upstream of Psyche and diverted around the magnetosphere, analogous to solar wind diversion about planetary magnetospheres.

Figures 1d–1f show the magnetic field, plasma density, and velocity in the *xy* plane, perpendicular to the IMF plane. The direction of the undisturbed solar wind proton gyromotion upstream of Psyche is clockwise in this plane. The solar wind proton gyroradius is nearly 15 times larger than the radius of Psyche and is comparable to the size of Psyche's magnetosphere in run #1, further validating the necessity of using a kinetic plasma simulation to study the interaction for the spatial scales introduced in run #1. As the particles interact with Psyche's magnetic field, some of them enter the magnetosphere and become subject to additional drift motions, including gradient and curvature drifts (e.g., Baumjohann & Treumann, 1996). The direction

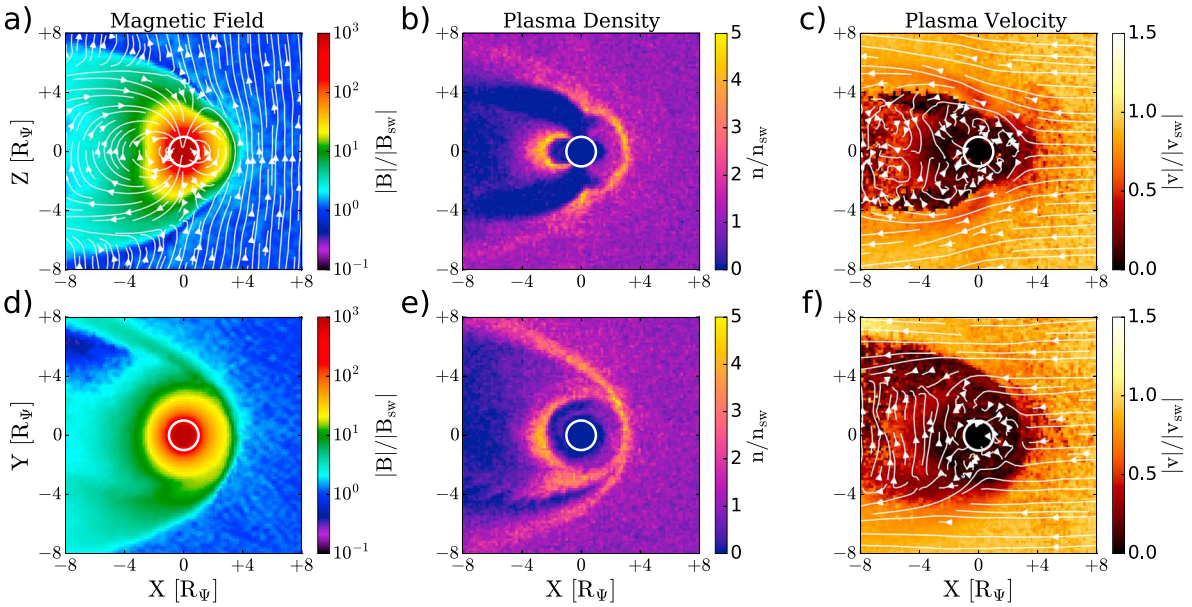

Figure 2. Hybrid simulation results for run #2 presented in Table 1 in the same format as Figure 1.

of gradient and curvature drift is consistent with the ion flow shown in Figure 1f and is more visible inside the magnetotail at close distances to Psyche. The plasma density enhancement inside Psyche's magnetosphere (Figure 1e) is also an indication for the quasi-trapped solar wind protons in Psyche's magnetosphere. The longitudinal drift motion of these ions, which also exists in terrestrial magnetospheres (e.g., Daglis et al., 1999), forms a partial ring current system that lies in the equatorial plane. Since the size of Psyche's magnetosphere is comparable to the upstream ion gyroradius, drifting quasi-trapped particles move toward the dayside magnetopause and are lost either by impacting the surface of Psyche or by crossing the magnetopause and emerging into the solar wind.

Figure 2 shows the hybrid simulation results for run #2, where the equatorial magnetic field is four times stronger than that in run #1. By comparing Figure 2 with Figure 1, we see that the global structure of the solar wind interaction with magnetized Psyche is qualitatively similar; however, since the strength of the intrinsic magnetic dipole moment in run #2 is larger than in run #1, the size of Psyche's magnetosphere is larger in run #2. Figure 2a shows that the magnetic field lines slightly bend upstream and around Psyche's magnetosphere, while the field lines remain relatively undisturbed upstream of the magnetopause in Figure 1a. Another notable difference is the appearance of the dayside trapped particles inside Psyche's magnetosphere (between Psyche and the upstream magnetopause), evident in Figure 2b. The local density of these trapped particles is nearly 50% of the undisturbed solar wind plasma density and is about an order of magnitude lower than the trapped particle density on the nightside. Figures 2c and 2f show that the solar wind plasma starts decelerating and diverting around the magnetosphere from $x < +6R_\Psi$ where its velocity reduces to nearly 30% of the upstream velocity at $x = +3R_\Psi$. Figure 2f shows that the plasma velocity in the quasi-trapped region at $x = -3R_\Psi$ is nearly 10% of the upstream velocity and continues increasing to over 50% at $x = -5R_\Psi$, mainly because of the curvature force, and then decelerates to ~20% at $x < -6R_\Psi$.

One notable feature, evident in Figures 1 and 2 for a magnetized Psyche, is the lack of an evident bow shock upstream of the magnetopause. Although the solar wind velocity has considerably decreased upstream of Psyche (e.g., Figures 1c and 2c) and there is a plasma density enhancement near the magnetopause (e.g., Figures 1b and 2b), we do not observe any clear signature of a bow shock in our simulations. Previously, it has been theoretically shown that a standing point distance larger than $\sim 20\delta_i$ is required for the formation of a bow shock upstream of a magnetized obstacle (Blanco-Cano et al., 2004; Omidi et al., 2004, 2005). The standing point distance is the point at which the solar wind pressure balances the magnetic pressure generated by a magnetized obstacle. In both run #1 and run #2, the standing point distance in our simulations is $< 3\delta_i$, which is much smaller than the minimum required distance ($\sim 20\delta_i$) to form a bow shock suggested by Blanco-Cano et al. (2004) and Omidi et al. (2004) and discussed by Simon et al. (2006).

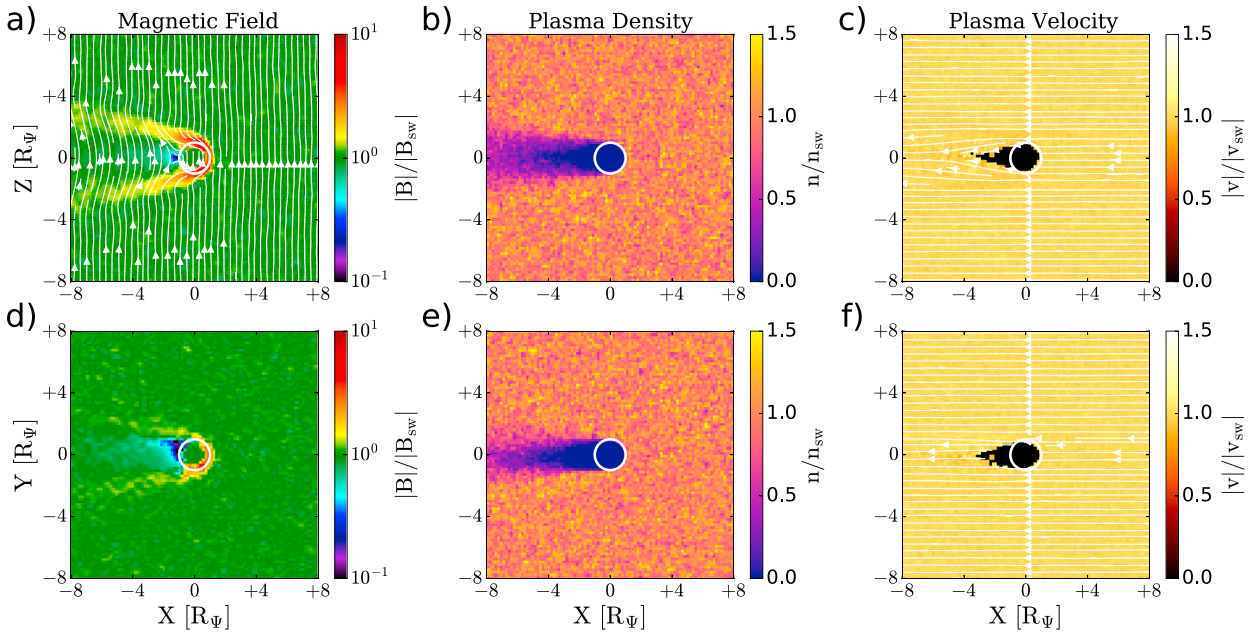

Figure 3. Hybrid simulation results for run #3 presented in Table 1. The description of each panel and geometry of the cuts are the same as those in Figure 1.

Figure 3 shows the hybrid model simulations assuming Psyche has no intrinsic magnetic dipole but is instead a conductive obstacle to the solar wind plasma (run #3 in Table 1). For simplicity, we initialized the simulation with uniform magnetic fields across the domain and kept all the solar wind parameters and the IMF orientation and strength constant in time at the upstream inflow boundary ($x = +8R_\Psi$). In this simulation, the convective electric field of the solar wind, $\mathbf{E} = -\mathbf{v} \times \mathbf{B}$, generates an electric current (a unipolar generator) inside Psyche, $\mathbf{J} = \sigma\mathbf{E}$, where $\sigma = 10$ S/m is the uniform conductivity for Psyche's interior in this simulation. This electric current, which is known as the toroidal current, induces a toroidal magnetic field (e.g., Schubert & Schwartz, 1969; 1969; Sonett & Colburn, 1968). Since the direction of this current inside Psyche is parallel to the electric field and is along the $-y$ axis in this simulation, the induced magnetic field is parallel (antiparallel) to the direction of the IMF upstream (downstream) of Psyche and increases (decreases) magnetic field intensity there, as shown in Figure 3a. We also see that the magnetic fields drape around the conductive body of Psyche.

Although not identical, similar signatures have been observed around other conductive obstacles in the solar system, for example, within Venus' ionosphere (e.g., Luhmann & Cravens, 1991). When a magnetized plasma interacts with a conducting unmagnetized obstacle that has a substantial internal conductivity (e.g., Europa) and/or a dense ionosphere (e.g., Venus), the incident plasma and magnetic field cannot penetrate into the conducting region; thus, they are slowed down upstream and diverted around the obstacle. As shown in Figure 3a, this prohibition for the magnetic field penetration into the conducting medium forms a magnetic pileup and field line draping around Psyche. However, due to the large conductivity of Psyche, magnetic diffusion time scale is on the order of tens of hours, which is much larger than the simulation time presented here ($t = 30$ s) and is beyond the capability of any three-dimensional kinetic plasma model to reach such time scales because kinetic models are computationally expensive. Thus, the simulation results presented in run #3 are a snapshot at a certain time (not a steady state) before allowing the magnetic diffusion process to settle and smooth out magnetic disturbances generated by the conductive interior of Psyche.

Figures 3b and 3e show a plasma cavity behind Psyche (known as a plasma wake) forming due to plasma absorption by Psyche's surface. As shown in Figure 3, the intensity of the induced magnetic fields are not high enough to considerably affect the solar wind plasma density and velocity. Previous plasma simulations of the solar wind interaction with unmagnetized atmosphereless bodies, like the Moon and a Saturnian satellite, Rhea, have reported a very similar plasma density structure in the wake of those objects (e.g., Fatemi et al., 2013; Holmström et al., 2012; Khurana et al., 2017; Poppe et al., 2014; Simon et al., 2012), which has been confirmed through observations (e.g., Khurana et al., 2017; Simon et al., 2012; Zhang et al., 2014, 2016). The structure of the plasma wake is predominately controlled by the orientation of the IMF with respect to

the solar wind plasma flow and the plasma beta (e.g., Ogilvie et al., 1996; Simon et al., 2012). However, if the induced magnetic fields of Psyche are larger than modeled here (due to higher internal conductivity), a magnetosphere-like structure may form, similar to the simulation results presented in Figure 1 or perhaps those in Figure 2.

Figures 3c and 3f show the magnitude of the plasma velocity, where we do not observe any significant plasma acceleration or deceleration associated with the interaction. This is in contrast with the plasma velocity observed in the wake of the Moon (e.g., see Holmström et al., 2012; Ogilvie et al., 1996; Zhang et al., 2014). However, considering the small size of Psyche relative to the ion thermal gyroradius ($R_\Psi \approx 0.7 r_{gi}$), and the small solar wind ion and electron thermal pressure near Psyche (~2 pPa for solar wind density 2 cm^{-3} and temperature 6 eV used in our simulations) compared to those around the Moon (~13.5 pPa for typical solar wind density ~7 cm^{-3} and temperature ~12 eV (e.g., Halekas et al., 2015; Holmström et al., 2012; Ogilvie et al., 1996), the solar wind ions can fill in the wake (thermal expansion) without being noticeably accelerated or decelerated by ambipolar electric field across Psyche's plasma wake compared to those in the lunar wake (e.g., Halekas et al., 2015; Nishino et al., 2009).

4. Discussion

Primitive bodies such as asteroids witness the various processes that have occurred during the solar system formation era. The interior properties of these bodies reflect their formation and subsequent evolution, yet much is still poorly understood, mainly due to the paucity of direct (in situ) observations of these objects. Using a GPU-based hybrid model of plasma, AMITIS, we have examined the solar wind plasma interaction of the M-type (metallic) asteroid 16 Psyche assuming two different magnetization scenarios, both of which are associated with distinct hypotheses for Psyche's formation. These results have important implications for the interpretation of magnetometer observations to be taken by the upcoming Psyche mission and any other future missions to metallic asteroids. We note that in this study we have only considered typical solar wind plasma condition near the orbit of Psyche with a northward IMF, while any variability in the solar wind magnetic field direction and strength as well as changes in solar wind plasma parameters (e.g., velocity, density, and temperature) will have direct impact on the solar wind interaction with Psyche, which would result in changing the structure of Psyche's magnetosphere and plasma environment.

Depending on the level of magnetization, the morphology of the solar wind plasma interaction with Psyche considerably changes. If Psyche is a nonconductive unmagnetized object, which is very unlikely, the interaction is more similar to a moon-like interaction where the solar wind plasma is absorbed by the surface and a plasma wake with a diamagnetic cavity forms downstream behind the object (e.g., Colburn et al., 1967; Fatemi et al., 2013; Halekas et al., 2015; Poppe et al., 2014; Zhang et al., 2014). If Psyche is weakly magnetized, similar to the simulation results presented in Figures 1 and 2, the interaction is similar to that with Mercury where a small dynamic magnetosphere forms (e.g., Kabin et al., 2000; Kallio & Janhunen, 2003; Raines et al., 2015; Richer et al., 2012). For a highly magnetized Psyche (larger than that modeled here), the interaction may become Earth-like, where a large magnetosphere forms with perhaps a bow shock upstream (e.g., Blanco-Cano et al., 2004; Omidi et al., 2002).

In addition, the solar wind interaction with Psyche also changes with the level of its interior conductivity. In this study, we presented, for the first time, the solar wind plasma interaction with an unmagnetized but conductive asteroid using a kinetic model (Figure 3). Although we did not present the interaction between a time-varying solar wind and IMF with a conductive Psyche, a preliminary analysis derived from Saur et al. (2010) has suggested that the induced magnetic fields generated by a time-varying IMF for a small-sized object like Psyche are weak ($\ll$5 nT) compared to either our assumed intrinsic values in runs #1 and #2 or the induced fields generated by the solar wind convective electric field in run #3. Thus, we have not included the changes of the IMF. In addition, Jia et al. (2015) have studied the effects of solar wind dynamic pressure enhancement in formation of an induced magnetosphere inside Mercury's magnetosphere generated by a large conductive interior of Mercury. According to simulations by Jia et al. (2015), a dynamic pressure enhancement from 11 nPa to 66 nPa can induce ~200 nT fields at the surface of Mercury and increase Mercury's surface field by a factor of 2. If we assume that such a large dynamic pressure reaches the orbit of Psyche (which would be rare), considering the fact that the conductive interior of Mercury (~2,000 km in radius e.g., Smith et al., 2012) is nearly 18 times larger than the average radius of Psyche, we do not expect induced magnetic field at the surface of Psyche to be larger than a few nanoteslas, which is negligible compared to a few hundreds or perhaps thousands

of nanoteslas intrinsic fields at the surface of Psyche. However, we note that various combinations of the IMF orientation relative to the solar wind flow direction, changes in the solar wind plasma and IMF, and Psyche's magnetic dipole moment strength and orientation have important effects on the solar wind interaction with Psyche, which are not the main focus of this paper and deserve a separate study.

In a majority of the previous modeling studies of plasma interaction with a magnetized asteroid, a very large dipole magnetization is assumed (a few tens of thousands of nanotesla surface fields) (e.g., Blanco-Cano et al., 2003; Kivelson et al., 1995; Wang et al., 1995), making the plasma interaction similar to the Earth. Exceptions include hybrid simulations presented by Omidi et al. (2002) and Simon et al. (2006). Omidi et al. (2002) obtained their simulation results from a two-dimensional hybrid model where their entire asteroid is covered with only one simulation grid cell. In addition, two-dimensional simulations, which model the body as an infinitely long cylinder (or a rectangular cube in Omidi et al., 2002 model), imply that the entire magnetosphere and bow shock have infinite length along the third dimension, which does not allow the solar wind magnetic fields to slip around the body and/or the magnetosphere, thus causing fields to pile up at the sunward side and exert greater pressure on the solar wind. In turn, the solar wind stagnation point is typically greater in two-dimensional simulations (i.e., Omidi et al., 2002) than in three-dimensional simulations, that is, those presented here. Simon et al. (2006), used a three-dimensional hybrid model; however, the radius of their asteroid, based on the parameters provided in their study, is ~1,350 km (~$7\delta_i$ or ~$10r_{gi}$, where $\delta_i \approx$192 km and thermal ion gyroradius $r_{gi} \approx$135 km in their simulations). This object size and its relative sizes to the solar wind plasma length scales are larger than the size of the largest asteroid (1 Ceres) in our solar system. Here as we explained in section 2.1, we presented the simulation results using a three-dimensional hybrid model with realistic length scales for Psyche, where the actual radius of Psyche is 120 km and it is covered with 12 simulation grid cells along its diameter.

If the magnetometer on board the Psyche mission observes a large coherent dipolar magnetic field around Psyche, the structure of Psyche's magnetosphere may be similar to that presented in Figures 1 and 2 (a Mercury-like interaction). Dipolar magnetic fields larger than those simulated here (i.e., one that generates surface fields on the order of 10^4 nT) may form a bow shock upstream of Psyche, making the interaction similar to that of the Earth (e.g., Omidi et al., 2002; Blanco-Cano et al., 2003). In turn, observation of a coherent dipole field would suggest that Psyche had a magnetic dynamo, perhaps as a planetesimal core. In contrast, if the magnetometer does not observe a dipolar magnetic field structure, the metallic and conductive body of Psyche should generate induced magnetic fields that perturb the magnetic field and plasma around Psyche, similar to the simulations presented in Figure 3.

Acknowledgments
The authors gratefully acknowledge support from NASA's Solar System Exploration Research Virtual Institute (SSERVI), grant NNX14AG16A. Data from the modeling results are available upon request to S. Fatemi.

References

Asphaug, E., Agnor, C. B., & Williams, Q. (2006). Hit-and-run planetary collisions. *Nature*, *439*, 155–160.
Auster, H. U., Richter, I., Glassmeier, K. H., Berghofer, G., Carr, C. M., & Motschmann, U. (2010). Magnetic field investigations during ROSETTA's 2867 Steins flyby. *Planetary and Space Science*, *58*(9), 1124–1128.
Banaszkiewicz, M., Seweryn, K., & Wawrzaszek, R. (2007). A sensor to perform in-situ thermal conductivity determination of cometary and asteroid material. *Advances in Space Research*, *40*(2), 226–237.
Baumgärtel, K., Sauer, K., & Bogdanov, A. (1994). A magnetohydrodynamic model of solar wind interaction with asteroid gaspra. *Science*, *263*(5147), 653–655.
Baumgärtel, K., Sauer, K., & Story, T. R. (1997). Solar wind response to a magnetized asteroid: Linear theory. *Icarus*, *129*, 94–105.
Baumjohann, W., & Treumann, R. A. (1996). *Basic space plasma physics*. London: Imperial College Press.
Bell, J. F., Davis, D. R., Hartmann, W. K., & Gaffey, M. J. (1989). Asteroids—The big picture. In R. P. Binzel, T. Gehrels, & M. S. Matthews (Eds.), *Asteroids II* (pp. 921–945). Tucson, AZ: University of Arizona Press.
Blanco-Cano, X., Omidi, N., & Russell, C. T. (2003). Hybrid simulations of solar wind interaction with magnetized asteroids: Comparison with Galileo observations near Gaspra and Ida. *Journal of Geophysical Research*, *108*(A5), 1216. https://doi.org/10.1029/2002JA009618
Blanco-Cano, X., Omidi, N., & Russel, C. T. (2004). How to make a magnetosphere. *Astronomy and Geophysics*, *45*(3), 3.14–3.17.
Bottke, W. F., Nesvorný, D., Grimm, R. E., Morbidelli, A., & O'Brien, D. P. (2006). Iron meteorites as remnants of planetesimals formed in the terrestrial planet region. *Nature*, *439*(7078), 821–824.
Britt, D. T., Yeomans, D., Housen, K., & Consolmagno, G. (2002). Asteroid density, porosity, and structure. In D. T. Britt, D. Yeomans, K. Housen, & G. Consolmagno (Eds.), *Asteroids III* (pp. 485–500). Tucson, AZ: The University of Arizona Press.
Colburn, D. S., Currie, R. G., Mihalov, J. D., & Sonett, C. P. (1967). Diamagnetic solar-wind cavity discovered behind moon. *Science*, *158*(3804), 1040–1042.
Daglis, I. A., Thorne, R. M., Baumjohann, W., & Orsini, S. (1999). The terrestrial ring current: Origin, formation, and decay. *Reviews of Geophysics*, *37*(4), 407–438.
Davis, D. R., Farinella, P., & Marzari, F. (1999). The missing Psyche family: Collisionally eroded or never formed? *Icarus*, *137*, 140–151.
Elkins-Tanton, L. T. (2016). Solar system smashup. *Scientific American*, *315*(6), 42–49.
Elkins-Tanton, L. T., Asphaug, E., Bell, J., Bercovici, D., Bills, B. G., Binzel, R. P., … Zuber, M. T. (2015). The discovery science of asteroid (16) Psyche. *46th Lunar and Planetary Science Conference, held March 16–20, 2015 in The Woodlands, Texas. LPI Contribution No. 1832* (1632 pp.).

Elkins-Tanton, L. T., Asphaug, E., Bell, J., Bercovici, D., Bills, B. G., Binzel, R. P., … Zuber, M. T. (2016). Asteroid (16) Psyche: The science of visiting a metal world. *47th Lunar and Planetary Science Conference, held March 21–25, 2016 at The Woodlands, Texas. LPI Contribution No. 1903* (1631 pp.).

Elkins-Tanton, L. T., Asphaug, E., Bell, J., Bercovici, D., Bills, B. G., Rinzel, R. P., … Zuber, M. T. (2017). Asteroid (16) Psyche: Visiting a metal world. *Lunar and Planetary Science Conference (LPSC) XLVIII, 20.-24. March 2017, The Woodlands, Texas, USA*.

Fatemi, S., Holmström, M., Futaana, Y., Barabash, S., & Lue, C. (2013). The lunar wake current systems. *Geophysical Research Letters*, *40*, 17–21. https://doi.org/10.1029/2012GL054635

Fatemi, S., Poppe, A. R., Delory, G. T., & Farrell, W. M. (2017). AMITIS: A 3D GPU-based hybrid-PIC model for space and plasma physics. *Journal of Physics: Conference Series*, *837*(1), 12017. https://doi.org/10.1088/1742-6596/837/1/012017

Fert, A., & Campbell, I. A. (1976). Electrical resistivity of ferromagnetic nickel and iron based alloys. *Journal of Physics F: Metal Physics*, *6*(5), 849–871.

Greenstadt, E. W. (1971). Conditions for magnetic interaction of asteroids with the solar wind. *Icarus*, *14*(3), 374–381.

Gomi, H., & Hirose, K. (2015). Electrical resistivity and thermal conductivity of hcp Fe-Ni alloys under high pressure: Implications for thermal convection in the Earth's core. *Physics of the Earth and Planetary Interiors*, *247*, 2–10.

Halekas, J. S., Brain, D. A., & Holmström, M. (2015). Moon's plasma wake. In J. S. Halekas, D. A. Brain, & M. Holmström (Eds.), *Magnetotails in the Solar System* (pp. 149–167). Hoboken, NJ: John Wiley.

Holmström, M., Fatemi, S., Futaana, Y., & Nilsson, H. (2012). The interaction between the Moon and the solar wind. *Earth, Planets and Space*, *64*(2), 237–245.

Jia, X., Slavin, J. A., Gombosi, T. I., Daldorff, L. K. S., Toth, G., & van der Holst, B. (2015). Global MHD simulations of Mercury's magnetosphere with coupled planetary interior: Induction effect of the planetary conducting core on the global interaction. *Journal of Geophysical Research: Space Physics*, *120*, 4763–4775. https://doi.org/10.1002/2015JA021143

Kaasalainen, M., Torppa, J., & Piironen, J. (2002). Models of twenty asteroids from photometric data. *Icarus*, *159*, 369–395.

Kabin, K., Gombosi, T. I., DeZeeuw, D. L., & Powell, K. G. (2000). Interaction of Mercury with the solar wind. *Icarus*, *143*(2), 397–406.

Kallio, E., & Janhunen, P. (2003). Modelling the solar wind interaction with Mercury by a quasi-neutral hybrid model. *Annals of Geophysics*, *21*(11), 2133–2145.

Kallio, E., Wurz, P., Killen, R., McKenna-Lawlor, S., Milillo, A., Mura, A., … Ip, W.-H. (2008). On the impact of multiply charged heavy solar wind ions on the surface of Mercury, the Moon and Ceres. *Planetary and Space Science*, *56*(11), 1506–1516.

Khurana, K. K., Fatemi, S., Lindkvist, J., Roussos, E., Krupp, N., Holmström, M., … Dougherty, M. K. (2017). The role of plasma slowdown in the generation of Rhea's Alfvén wings. *Journal of Geophysical Research: Space Physics*, *122*(2), 1778–1788. https://doi.org/10.1002/2016JA023595

Kivelson, M. G., Wang, Z., Joy, S., Khurana, K. K., Polanskey, C., Southwood, D. J., & Walker, R. J. (1995). Solar wind interaction with small bodies: 2. What can Galileo's detection of magnetic rotations tell us about Gaspra and Ida. *Advances in Space Research*, *16*(4), 59–68.

Ledvina, S. A., Ma, Y.-J., & Kallio, E. (2008). Modeling and simulating flowing plasmas and related phenomena. *Space Science Reviews*, *139*(1–4), 143–189.

Lindkvist, J., Holmström, M., Fatemi, S., Wieser, M., & Barabash, S. (2017). Ceres interaction with the solar wind. *Research Letters*, *44*, 2070–2077. https://doi.org/10.1002/2016GL072375

Luhmann, J. G., & Cravens, T. E. (1991). Magnetic fields in the ionosphere of Venus. *Space Science Reviews*, *55*(1), 201–274.

Lupishko, D. F. (2006). On the bulk density of the M-type asteroid 16 Psyche. *Solar System Research*, *40*(3), 214–218.

Magri, C., Ostro, S. J., Rosema, K. D., Thomas, M. L., Mitchell, D. L., Campbell, D. B., … Yeomans, D. K. (1999). Mainbelt asteroids: Results of Arecibo and goldstone radar observations of 37 objects during 1980–1995. *Icarus*, *140*(2), 379–407.

Matter, A., Delbo, M., Carry, B., & Ligori, S. (2013). Evidence of a metal-rich surface for the Asteroid (16) Psyche from interferometric observations in the thermal infrared. *Icarus*, *226*(1), 419–427.

Nishino, M. N., Maezawa, K., Fujimoto, M., Saito, Y., Yokota, S., Asamura, K., … Shimizu, H. (2009). Pairwise energy gain-loss feature of solar wind protons in the near-Moon wake. *Geophysical Research Letters*, *36*, L12108. https://doi.org/10.1029/2009GL039049

Ogilvie, K. W., Steinberg, J. T., Fitzenreiter, R. J., Owen, C. J., Lazarus, A. J., Farrell, W. M., & Torbert, R. B. (1996). Observations of the lunar plasma wake from the WIND spacecraft on December 27, 1994. *Geophysical Research Letters*, *23*(10), 1255–1258.

Oh, D. Y., Goebel, D. M., Elkins-Tanton, L., Polanskey, C., Lord, P., Tilley, S., … Landau, D. (2016). Psyche: Journey to a metal world. In *52nd AIAA/SAE/ASEE Joint Propulsion Conference* (pp. 1–12). Big Sky, MT.

Omidi, N., Blanco-Cano, X., Russell, C. T., Karimabadi, H., & Acuna, M. H. (2002). Hybrid simulations of solar wind interaction with magnetized asteroids: General characteristics. *Journal of Geophysical Research*, *107*(A12), 1487. https://doi.org/10.1029/2002JA009441

Omidi, N., Blanco-Cano, X., & Russell, C. T. (2005). Macrostructure of collisionless bow shocks: 1. Scale lengths. *Journal of Geophysical Research*, *110*, A12212. https://doi.org/10.1029/2005JA011169

Omidi, X., Blanco-Cano, X., Russell, C. T., & Karimabadi, H. (2004). Dipolar magnetospheres and their characterization as a function of magnetic moment. *Advances in Space Research*, *33*(11), 1996–2003.

Poppe, A. R., Fatemi, S., Halekas, J. S., Holmström, M., & Delory, G. T. (2014). ARTEMIS observations of extreme diamagnetic fields in the lunar wake. *Geophysical Research Letters*, *41*(11), 3766–3773. https://doi.org/10.1002/2014GL060280

Raines, J. M., DiBraccio, G. A., Cassidy, T. A., Delcourt, D. C., Fujimoto, M., Jia, X., … Wurz, P. (2015). Plasma sources in planetary magnetospheres: Mercury. *Space Science Reviews*, *192*(1), 91–144.

Richer, E., Modolo, R., Chanteur, G. M., Hess, S., & Leblanc, F. (2012). A global hybrid model for Mercury's interaction with the solar wind: Case study of the dipole representation. *Journal of Geophysical Research*, *117*, A10228. https://doi.org/10.1029/2012JA017898

Richter, I., Auster, H. U., Glassmeier, K. H., Koenders, C., Carr, C. M., Motschmann, U., … McKenna-Lawlor, S. (2012). Magnetic field measurements during the ROSETTA flyby at asteroid (21)Lutetia. *Planetary and Space Science*, *66*(1), 155–164.

Russell, C. T. (1979). The interaction of the solar wind with Mars, Venus, and Mercury. In C. Russell (Ed.), *Solar system plasma physics* (Vol. 2, pp. 207–252). Amsterdam: North-Holland Publishing Co.

Saur, J., Neubauer, F. M., & Glassmeier, K.-H. (2010). Induced magnetic fields in solar system bodies. *Space Science Reviews*, *152*, 391–421.

Schubert, G., & Schwartz, K. (1969). A theory for the interpretation of lunar surface magnetometer data. *The Moon*, *1*, 106–117.

Shepard, M. K., Clark, B. E., Nolan, M. C., Howell, E. S., Magri, C., Giorgini, J. D., … Rivkin, A. (2008). A radar survey of M- and X-class asteroids. *Icarus*, *195*(1), 184–205.

Shepard, M. K., Clark, B. E., Ockert-Bell, M., Nolan, M. C., Howell, E. S., Magri, C., … Mueller, M. (2010). A radar survey of M- and X-class asteroids II. Summary and synthesis. *Icarus*, *208*(1), 221–237.

Shepard, M. K., Richardson, J., Taylor, P. A., Rodriguez-Ford, L. A., Conrad, A., de Pater, I., … Harris, A. W. (2017). Radar observations and shape model of asteroid 16 Psyche. *Icarus*, *281*, 388–403.

Simon, S., Bagdonat, T., Motschmann, U., & Glassmeier, K.-H. (2006). Plasma environment of magnetized asteroids: A 3-D hybrid simulation study. *Annales Geophysicae*, *24*, 407–414.

Simon, S., Kriegel, H., Saur, J., Wennmacher, A., Neubauer, F. M., Roussos, E., … Dougherty, M. K. (2012). Analysis of Cassini magnetic field observations over the poles of Rhea. *Journal of Geophysical Research*, *117*, A07211. https://doi.org/10.1029/2012JA017747

Smith, D. E., Zuber, M. T., Phillips, R. J., Solomon, S. C., Hauck, II S. A., Lemoine, F. G., … Taylor, A. H. (2012). Gravity field and internal structure of Mercury from MESSENGER. *Science*, *336*(6078), 214–217.

Sonett, C. P., & Colburn, D. S. (1968). The principle of solar wind induced planetary dynamos. *Physics of the Earth and Planetary Interiors*, *1*(5), 326–346.

Stacey, F. D., & Anderson, O. L. (2001). Electrical and thermal conductivities of Fe-Ni-Si alloy under core conditions. *Physics of the Earth and Planetary Interiors*, *124*(3), 153–162.

Viateau, B. (2000). Mass and density of asteroids (16) Psyche and (121) Hermione. *Astronomy and Astrophysics*, *354*, 725–731.

Wang, Z., & Kivelson, M. G. (1996). Asteroid interaction with solar wind. *Journal of Geophysical Research*, *101*(A11), 24,479–24,493.

Wang, Z., Kivelson, M. G., Joy, S., Khurana, K. K., Polanskey, C., Southwood, D. J., & Walker, R. J. (1995). Solar wind interaction with small bodies: 1. Whistler wing signatures near Galileo's closest approach to Gaspra and Ida. *Advances in Space Research*, *16*(4), 47–57.

Weiss, B. P., Bryson, J. F., Harrison, R. J., Neufeld, J. A., Elkins-Tanton, L. T., Russell, C. T., … Kronast, F. (2016). A core dynamo on an iron meteorite parent body and the magnetism of metallic asteroids. *47th Lunar and Planetary Science Conference, 1661*.

Zellner, B., & Gradie, J. (1976). Minor planets and related objects. XX—Polarimetric evidence for the albedos and compositions of 94 asteroids. *Astronomical Journal*, *81*, 262–280.

Zhang, H., Khurana, K. K., Kivelson, M. G., Angelopoulos, V., Wan, W. X., Liu, L. B., … Liu, W. L. (2014). Three-dimensional lunar wake reconstructed from ARTEMIS data. *Journal of Geophysical Research: Space Physics*, *119*, 5220–5243. https://doi.org/10.1002/2014JA020111

Zhang, H., Khurana, K. K., Kivelson, M. G., Fatemi, S., Holmström, M., Angelopoulos, V., … Liu, W. L. (2016). Alfvén wings in the lunar wake: The role of pressure gradients. *Journal of Geophysical Research: Space Physics*, *121*, 10,698–10,711. https://doi.org/10.1002/2016JA022360

Zimmerman, M. I., Farrell, W. M., & Poppe, A. R. (2014). Grid-free 2D plasma simulations of the complex interaction between the solar wind and small, near-Earth asteroids. *Icarus*, *238*, 77–85.